

APPENDIX

"Association of the unusual GTPase IFT22 with the IFT complex is required for flagellum construction" by Wachter et al.,

TABLE OF CONTENT:

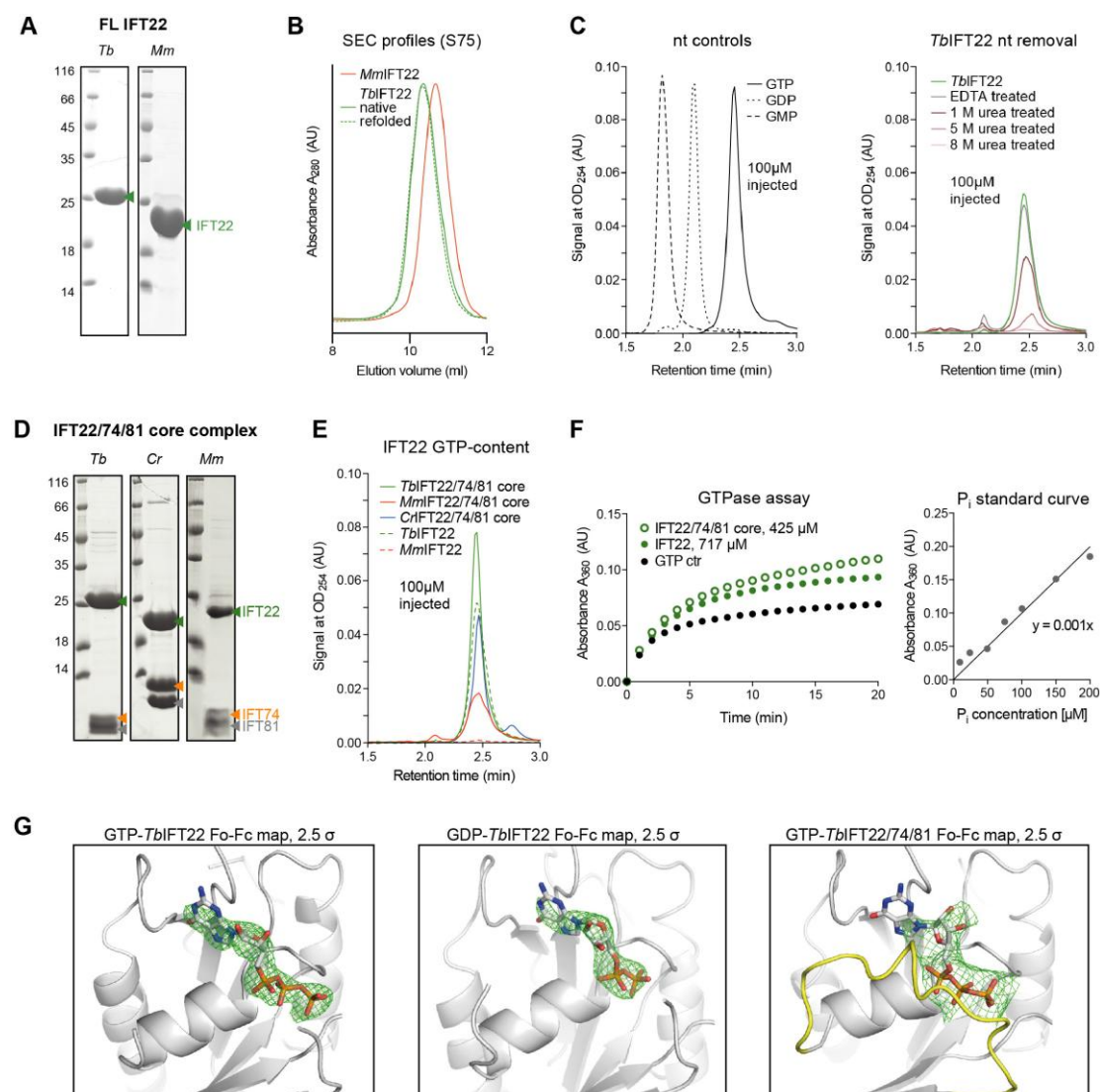
Appendix Text: page 2

Appendix Figures and Legends S1-S7: Page 3-14

Appendix text: Analysis of GFP::IFT22 in *T. brucei*

GFP::IFT22 was previously shown to traffic in the trypanosome flagellum (Adhiambo *et al*, 2009), but conditions for proper quantification were not available at the time. We therefore acquired videos of GFP::IFT22 trafficking and quantified the movement by kymograph analysis (Buisson *et al*, 2013). Anterograde movement of GFP::IFT22 occurred at a frequency of 0.84 s^{-1} and at an average speed of $2.73 \pm 0.69\text{ }\mu\text{m/s}$ ($n = 218$). These values are in the same range as observed for GFP::IFT27 (Huet *et al*, 2014) or GFP::IFT52 (Buisson *et al*, 2013). RNAi silencing of IFT22 surprisingly resulted in a defect of retrograde transport (Adhiambo *et al*, 2009). To confirm this phenotype was specific and not due to an off-target effect, an RNAi-resistant version of IFT22 was fused to GFP (GFP::IFT22_{rescue}) to discriminate it from the product of the endogenous gene and expressed in the *IFT22*^{RNAi} cell line (Fig. S6A). For the sake of simplicity, this *IFT22*^{RNAi}+GFP::IFT22 RNAi resistant cell line will be called IFT22R. Western blot analysis using an antiserum against IFT22 demonstrated that the GFP::IFT22_{rescue} fusion protein displayed the expected motility on gel (expected MW of 52 kDa) and was detected alongside the endogenous protein (expected MW of 24 kDa) (Fig. S6B). Video-microscopy on live cells demonstrated typical IFT trafficking (Appendix video S1). Addition of tetracycline triggered RNAi knockdown of the endogenous IFT22 with the same efficiency as in the *IFT22*^{RNAi} cell line alone (Fig. S6B) and, as expected, the GFP::IFT22_{rescue} fusion protein was not affected (Fig. S6B, last lane). This result was confirmed in live cells (Appendix video S2). Of note, the signal-to-noise ratio for GFP-IFT22_{rescue} in the flagellum was better in induced conditions, indicating a competition with the endogenous untagged IFT22 protein. Immunofluorescence assays (IFA) with an anti-IFT172 monoclonal antibody and a marker of the axoneme were used to further characterize the phenotypes (Fig. 6B). As expected, knockdown of IFT22 in the *IFT22*^{RNAi} cell line led to the emergence of cells with tiny flagella usually filled with IFT material (Fig. 6B, second row), as previously reported (Adhiambo *et al*, 2009). By contrast, expression of the GFP::IFT22_{rescue} rescued the phenotype as these cells displayed normal IFT distribution and possess flagella of normal length (Fig. 6B, third row). These results formally prove that the phenotype is indeed due to IFT22 knockdown and not to off-target effects and demonstrate that IFT22 is a *bona fide* IFT protein that is essential for retrograde transport.

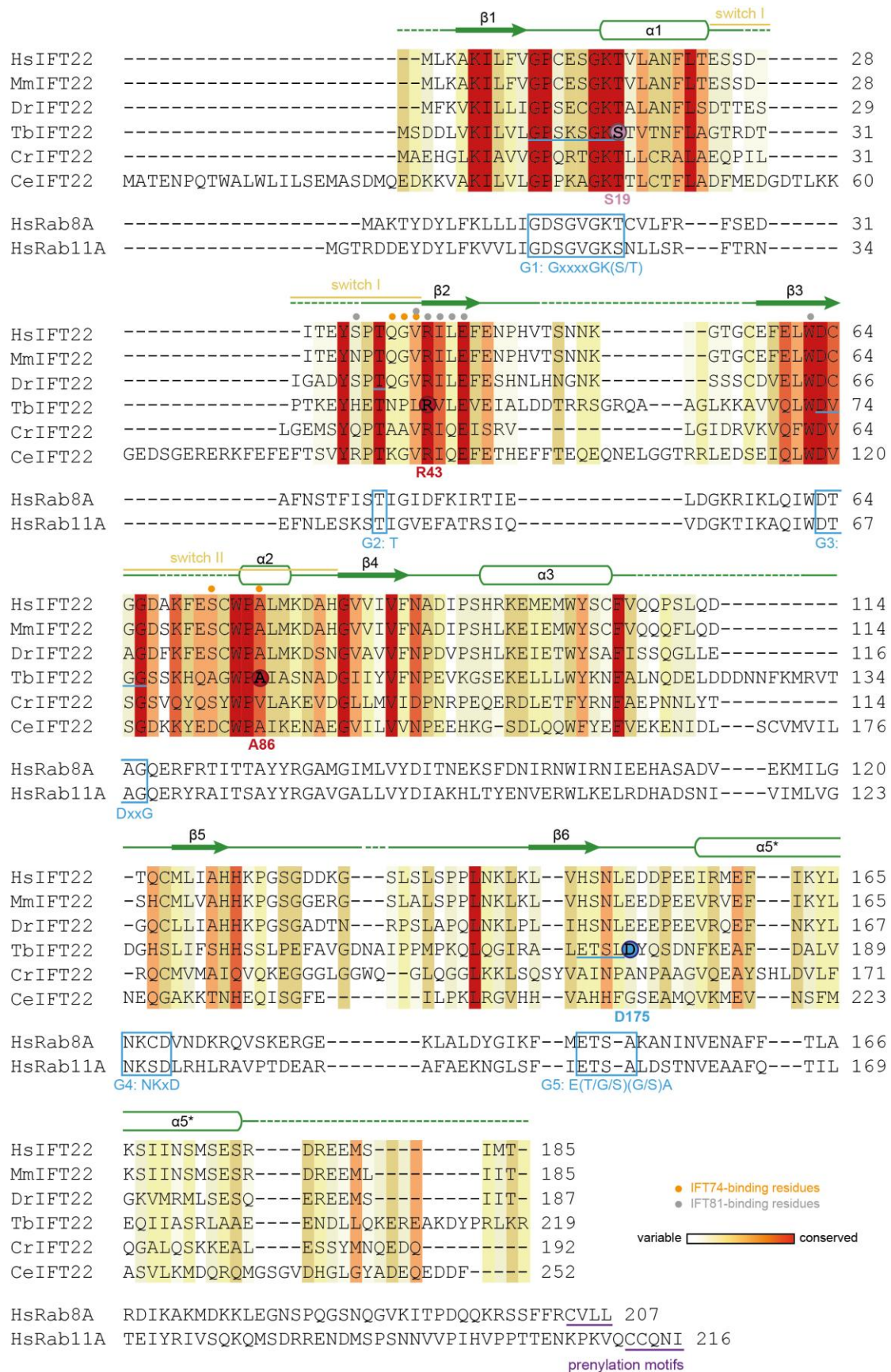
Appendix supplemental figures



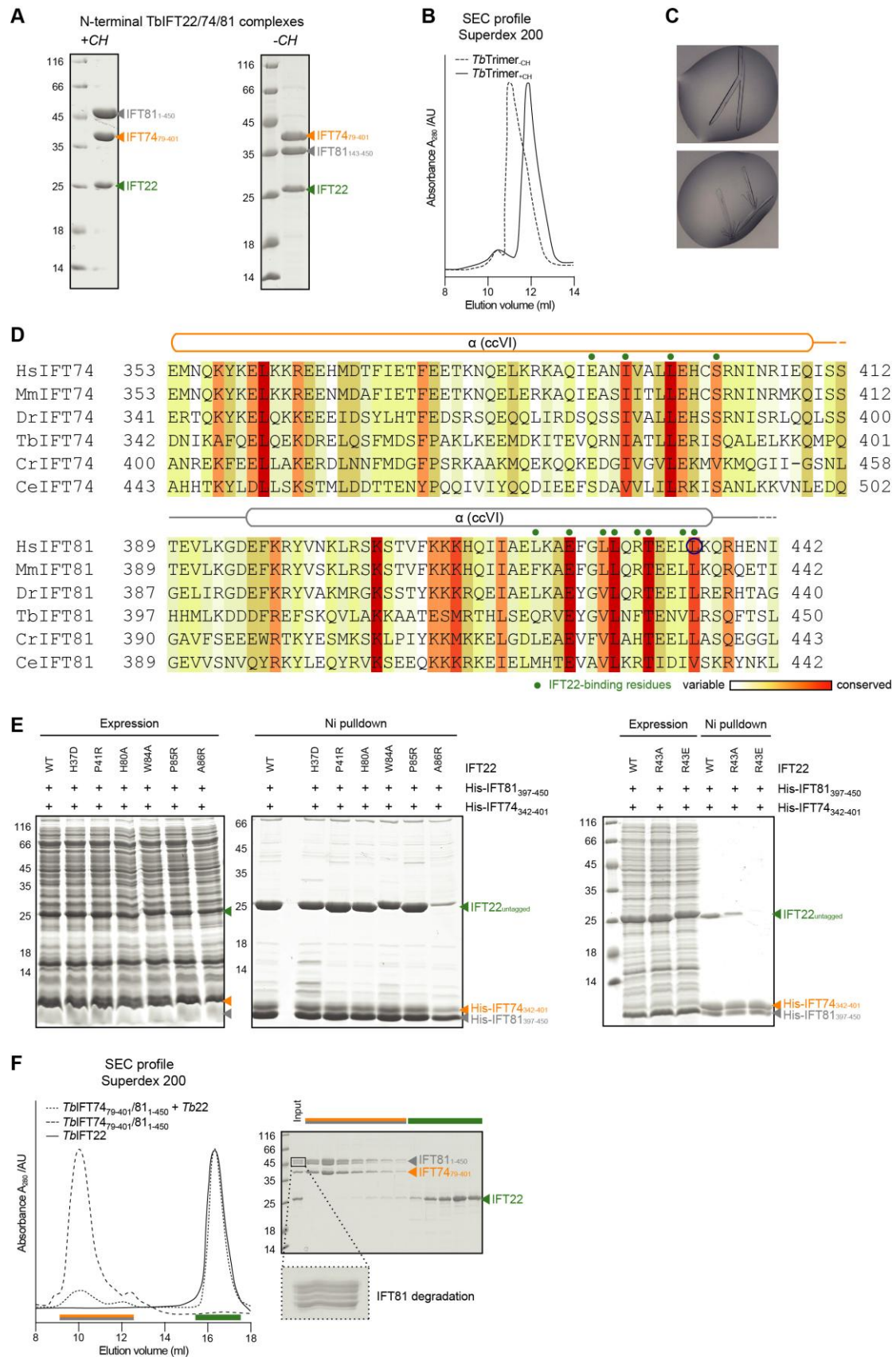
Appendix Figure S1: IFT22 nucleotide analysis

- A.** SDS-PAGE gels of purified IFT22 from *T. brucei* and *M. musculus*. (FL = full-length)
- B.** SEC profiles of TblIFT22 and MmlIFT22. The SEC elution profiles for both native and refolded TblIFT22 are shown in different shades of green.
- C.** HPLC nucleotide-elution profiles. Left: Nucleotide controls confirming that different G-nucleotides can be resolved. Right: Comparison of different procedures for nucleotide removal to obtain nucleotide-free IFT22. Treatment with 8 M urea effectively removed GTP carried along through co-purification from *E. coli* extracts.

- D.** SDS-PAGE gels of purified IFT22/74/81 core complexes from different organisms. IFT74/81 constructs were designed based on sequence alignments (see Fig. S3D) and resulting complexes are *TbIFT22/74*₃₄₂₋₄₀₁/*81*₃₉₇₋₄₅₀, *CrIFT22/74*₃₉₈₋₄₅₉/*81*₃₉₀₋₄₄₂, *MmIFT22/74*₃₅₂₋₄₀₆/*81*₃₈₉₋₄₄₁.
- E.** HPLC GTP-elution profiles of the indicated purified IFT22 proteins and IFT22/74/81 core complexes from different organisms. Same amounts of each protein (complex) were injected (20 μ l, 100 μ M).
- F.** GTPase activity assay for *TbIFT22* and the *TbIFT22/74/81* core complex. The release of inorganic Phosphate (P_i) upon addition of 1 mM GTP to the proteins was followed for 20 min. As a negative control, hydrolysis of 1 mM GTP in buffer was monitored and subtracted from the protein curves for rate quantifications (left image). GTPase activity rates (*TbIFT22*: $1.7 \times 10^{-3} \text{ min}^{-1}$; *TbIFT22/74/81* core: $4.7 \times 10^{-3} \text{ min}^{-1}$) were calculated based on a linear standard curve generated from different P_i concentrations (right image).
- G.** Unbiased Fo-Fc electron density maps (green, 2.5 \AA) of IFT22-bound nucleotides for structures solved in this study. IFT22 is shown in grey in cartoon representation in similar orientations for each structure and nucleotides are depicted as sticks.

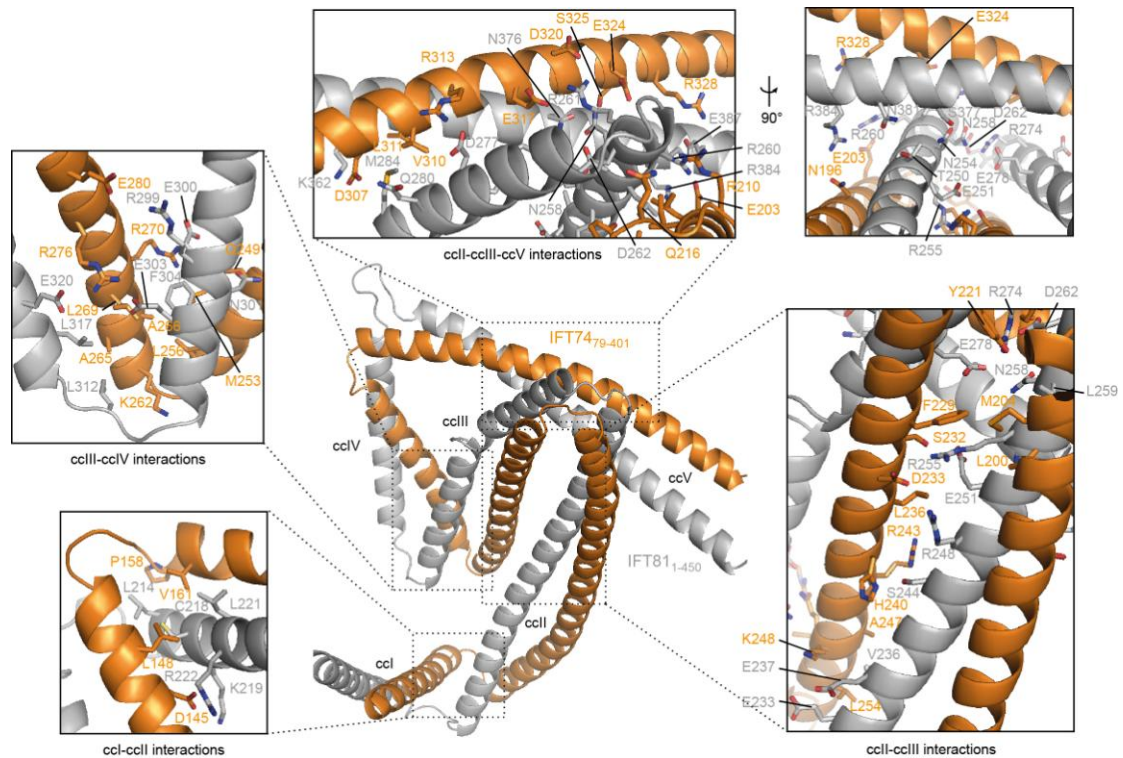


different organisms and the classical Rab GTPases Rab8A and Rab11A from *H. sapiens*. Surface conservation is shown according to ConSurf grades (only for IFT22 sequences). Secondary structure elements from the GTP-*Tb*IFT22 crystal structure (green and yellow) are indicated above the sequence, as are residues interacting with IFT74 (orange dots) and IFT81 (grey dots). Conserved sequence motifs of small GTPases are marked with blue boxes with consensus sequences inscribed below. Residues mutated in this study are encircled. (*Hs* = *Homo sapiens*, *Mm* = *Mus musculus*, *Dr* = *Danio rerio*, *Tb* = *Trypanosoma brucei*, *Cr* = *Chlamydomonas reinhardtii* and *Ce* = *Caenorhabditis elegans*)



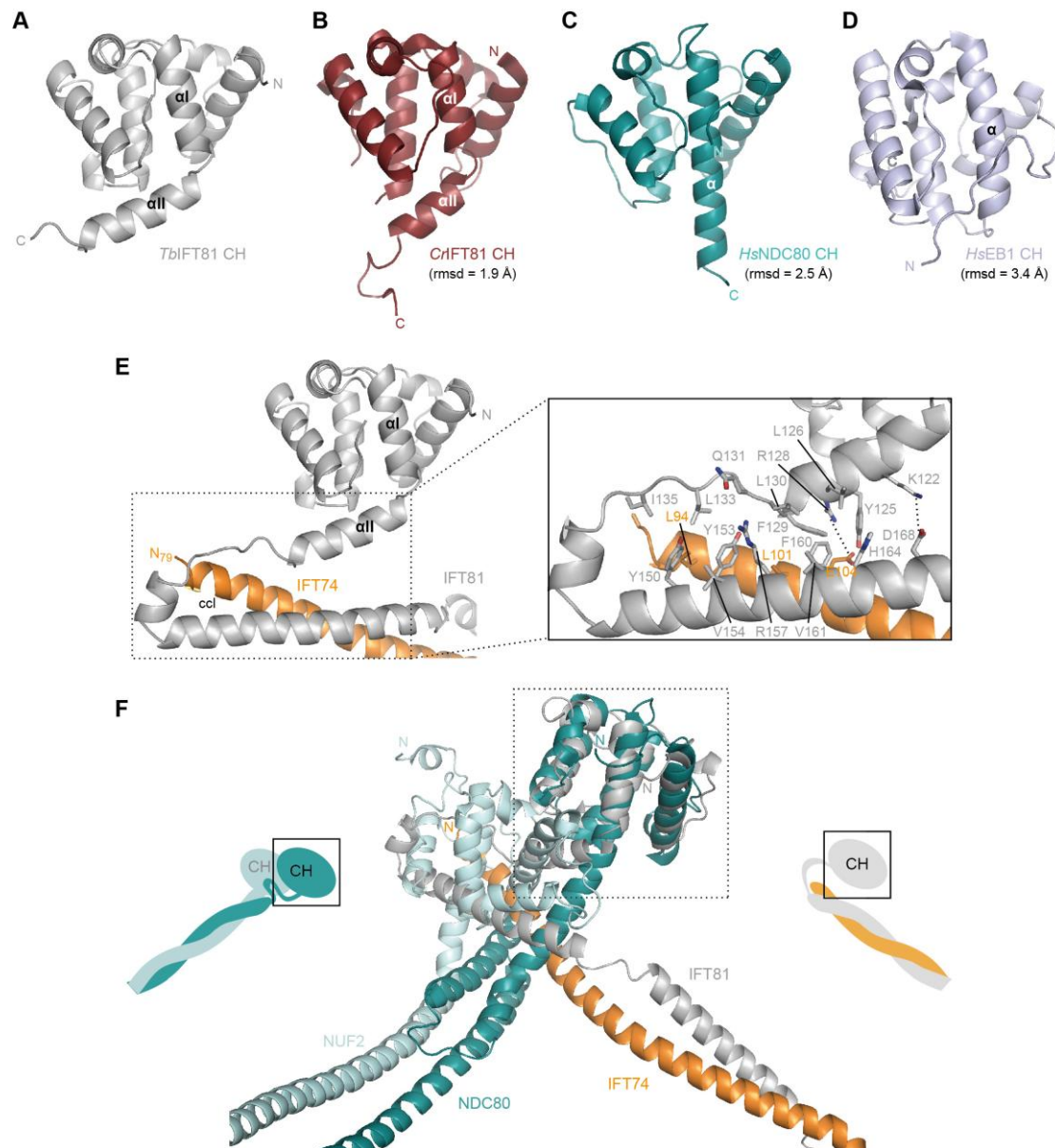
Appendix Figure S3: Probing the IFT22-74/81 interface

- A.** SDS-PAGE gels of purified *b*IFT22/74₇₉₋₄₀₁/81_{x-450} complexes with (left, x = 1) and without (right, x = 143) IFT81 CH domain. Only the complex with CH domain crystallized.
- B.** SEC profiles for the *Tb*IFT22/74₇₉₋₄₀₁/81₁₋₄₅₀ and *Tb*IFT22/74₇₉₋₄₀₁/81₁₄₃₋₄₅₀ complex.
- C.** *Tb*IFT22/74₇₉₋₄₀₁/81₁₋₄₅₀ crystals. Crystallization solution: 15% (v/v) glycerol, 7.5% (w/v) PEG4000 and 100 mM HEPES pH 7.5.
- D.** Clustal Omega multiple sequence alignment of the IFT22-binding region of homologous IFT74 and IFT81 sequences from different organisms. Surface conservation is shown according to ConSurf grades. Secondary structure elements from the IFT22/74/81 crystal structure are indicated above the sequence, as well as residues interacting with IFT22 (green dots). *Tetrahymena* and *Giardia* are organisms lacking an IFT22 homolog. (*Hs* = *Homo sapiens*, *Mm* = *Mus musculus*, *Dr* = *Danio rerio*, *Tb* = *Trypanosoma brucei*, *Cr* = *Chlamydomonas reinhardtii* and *Ce* = *Caenorhabditis elegans*, *Tt* = *Tetrahymena thermophila*, *Gi* = *Giardia intestinalis*).
- E.** Co-expression and Ni-NTA pulldown of WT and various *Tb*IFT22 mutants with *Tb*IFT74₃₄₂₋₄₀₁/81₃₉₇₋₄₅₀ core complexes. Figure panels labeled ‘Expression’ shows the total expression demonstrating that all IFT22 mutants are strongly expressed. The panels labeled ‘Ni pulldown’ demonstrate that some of the IFT22 point mutants are no longer able to interact with IFT74/81 core complexes.
- F.** (left) SEC profiles of *Tb*IFT22, *Tb*IFT22/74₇₉₋₄₀₁/81₁₋₄₅₀ and *Tb*IFT22 incubated with *Tb*IFT22/74₇₉₋₄₀₁/81₁₋₄₅₀ prior to SEC. (right) SDS-PAGE of the fractions from the SEC elution of ‘*Tb*IFT22/74₇₉₋₄₀₁/81₁₋₄₅₀ + *Tb*IFT22’ shows that IFT22 does not associate with the core complex, which is in contrast to co-expressed *Tb*IFT22/74₇₉₋₄₀₁/81₁₋₄₅₀. The zoom-in box shows that IFT81₁₋₄₅₀ has been partly degraded giving rise to at least 3 additional bands on the SDS-PAGE corresponding to 1-3kDa smaller size of IFT81 (confirmed by MS).



Appendix Figure S4: Interactions between coiled-coil regions of the IFT74/81 complex.

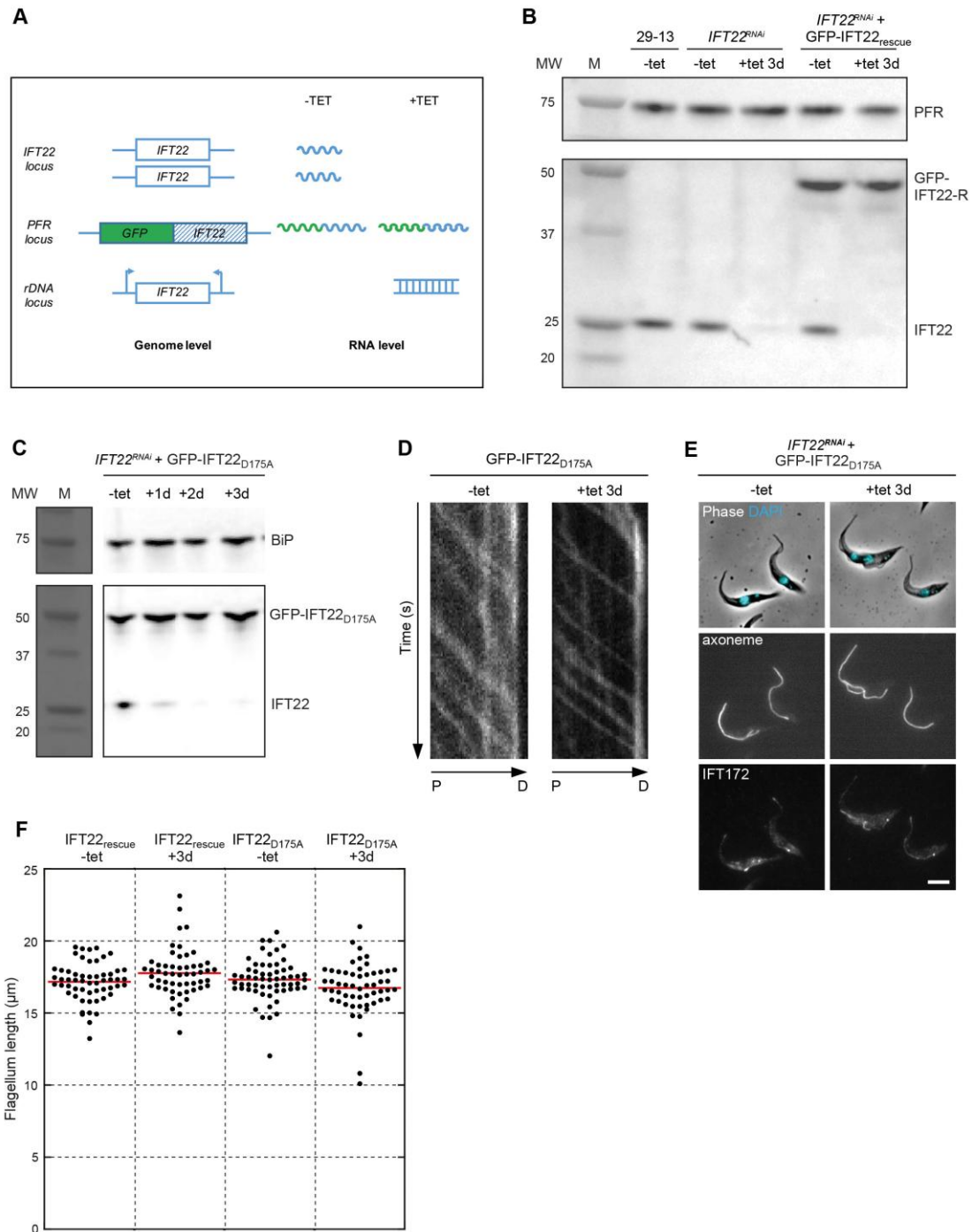
Cartoon representation of the *Tb*IFT74/81 coiled-coil scaffold (center). Dashed boxes indicate four distinct regions of interaction between the different coiled-coils: ccl-ccII, ccII-ccIII, ccIII-ccIV and ccII-ccIII-ccV. Zoomed-in views show interacting residues in stick representation.



Appendix Figure S5: Structural comparison of different microtubule-binding CH domains.

- A.** Cartoon representation of the crystal structure of the *TbIFT81* CH domain with the unusual C-terminal helices α I and α II labeled.
- B.** Cartoon representation of the crystal structure of the *CrIFT81* CH domain (PDB ID: 4lvp) with a similar C-terminal helix orientation.
- C-D.** Cartoon representation of the crystal structures of the microtubule-binding CH domains of *HsNDC80* (PDB ID: 3iz0) and *HsEB1* (PDB ID: 3co1). All structures are shown in the same orientation after superpositioning onto the *TbIFT81* CH domain. The rmsd for each superposition is indicated.

- E.** Left: Cartoon representation of the relative position of α II helix and ccI that tethers the IFT81 CH domain onto coiled coil region ccI. Right: Zoomed-in view of interacting residues of α II and ccI.
- F.** Cartoon representation of IFT74/81 and NDC80/NUF2 after superimposing the N-terminal CH domains (dashed box). While the IFT81 CH domain interacts with the coiled-coil moiety of the IFT74/81 heterodimer, the NDC80 CH domain is fixed through interactions with the NUF2 CH domain resulting in different overall architectures of the two complexes.

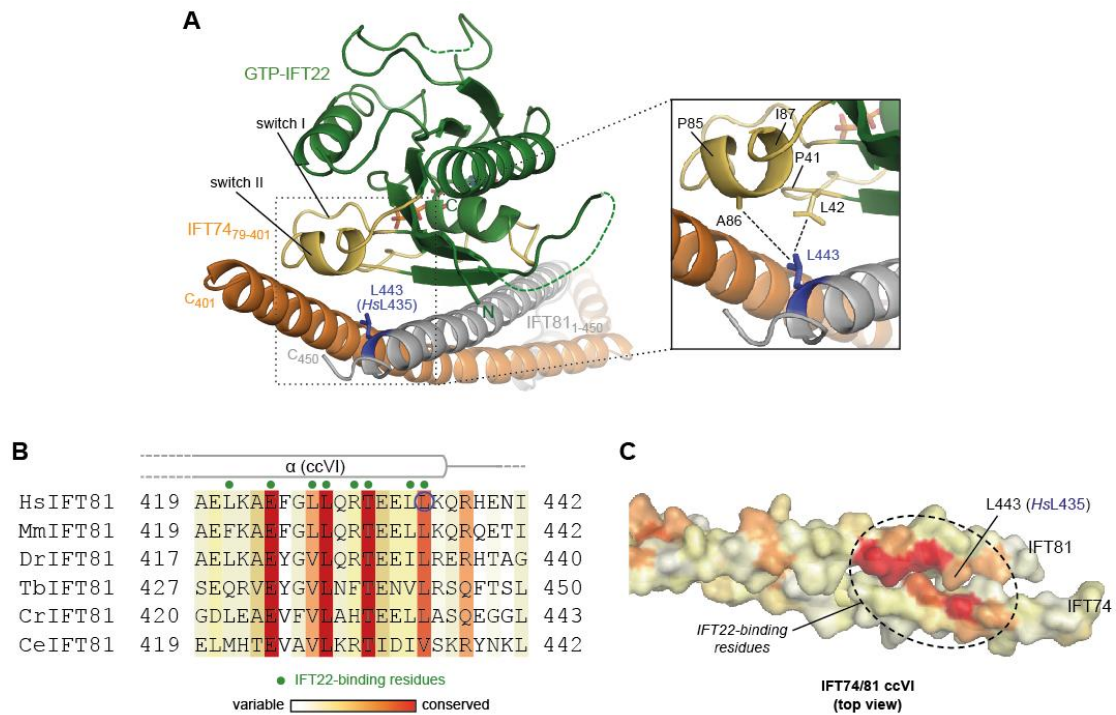


Appendix Figure S6: *In vivo* analysis of the IFT22_{D175A} in *Trypanosoma brucei*

A. Strategy used to evaluate the biological significance of IFT22 mutations. Boxes represent coding sequences and undulated lines correspond to mRNA. Cell lines used contain the two endogenous copies (trypanosomes are diploid) of *IFT22*, a single copy of an RNAi-resistant version (dashed blue) fused to GFP (green) expressed from the *PFR* (paraflagellar rod, a well-characterised flagellar gene, Bastin *et al* 1998) locus and a construct for expression of double-stranded *IFT22*

RNA under the control of tetracycline-inducible promoters. In the absence of tetracycline, there is no dsRNA and mRNAs originating from all three genes are present. However, addition of tetracycline triggers the production of dsRNA that result in degradation of transcripts from the endogenous genes but not from the recoded one.

- B.** Western blot analysis of the indicated cell lines probed with the anti-IFT22 antibody (bottom) and with an anti-PFR as loading control (top).
- C.** Western blot analysis of the *IFT22^{RNAi}+GFP::IFT22_{D175A}* cell line probed with the anti-IFT22 antibody (bottom) and with an anti-BiP as loading control (top). These samples were loaded on a blot together with the samples shown in Fig. 6A and thus share the same lane for molecular markers.
- D.** Kymographs showing the movement of the GFP::IFT22_{D175A} in the presence (left) or the absence (right) of endogenous IFT22. Note the improved signal-to-noise ratio in the latter case.
- E.** IFA in the indicated conditions using the mAb25 (marker for the axoneme, middle panels) and an anti-IFT172 antibody (marker for IFT, bottom panels). The top panels show the phase contrast image merged with DAPI (cyan) that stains nuclear and mitochondrial DNA. Scale bar is 5 μ m.
- F.** Dot plot representation of flagellum length in the indicated cell lines and conditions.



Appendix Figure S7: Ciliopathy-causing mutation of a conserved IFT81 leucine is located in the IFT22 binding site.

- A.** Mapping of *Hs*IFT81 L435 onto the *Tb*IFT22/74/81 structure reveals that the corresponding L443 in *Tb*IFT81 is located right in the interface with IFT22 making several hydrophobic interactions (see displayed interactions in the box to the right).
- A.** Sequence alignment of IFT81 residues from different organisms interacting with IFT22. The patient mutation L435 is encircled in blue and is a conserved leucine residue.
- C.** Surface conservation display of the IFT74/81 region interacting with IFT22 showing that L443 is part of a conserved IFT22-binding site.